Optimal Design of an Outer-Stator Magnetically Geared Permanent Magnet Machine

P.M. Tlali, *Member,* S. Gerber, *Member,* and R-J. Wang, *Senior Member, IEEE*

In this paper, a magnetically geared permanent magnet (MGPM) machine is proposed for use in wind power generation. The structure layout, operating principles and equivalent circuit of the MGPM machine are first described. Then an efficient finite element method (FEM) based design optimization approach is formulated and implemented in the design of the machine. The optimized machine shows that a rated torque density close to 70 kNm/m^3 can be achieved, which is significantly higher than that of conventional electrical machines. Furthermore, a prototype machine based on the design is constructed and experimentally evaluated. The measured torque performance shows a good agreement with the predicted one, but a significant difference exists between the measured and calculated efficiencies. This is mainly due to the higher than expected mechanical losses in the MGPM machine. Relevant conclusions are drawn based on the analysis of presented results and some key design related aspects.

***Index Terms*—Magnetic gears, magnetic flux modulation, permanent magnet, special electrical machines.**

I. Introduction

In the wind power industry, the mechanically geared wind turbine power-train consisting of a mechanical gearbox and a medium or high speed machine is often employed. These geared wind turbine systems exhibit certain advantages such as high generator efficiency and light weight [1], [2]. However, because of their intrinsic contact mechanism, mechanical gears are prone to friction losses, teeth wearing and are likely to be permanently damaged if overloaded. Frequent maintenance is thus needed as gearbox failures lead to both high repairing costs and extended down-times. As an alternative, directly driven generators (DDGs) are sometimes preferred over mechanically geared generator concepts due to their lower part count, simplicity and higher reliability prospects. Nevertheless, for large wind turbine systems characterized with low speed and high torque, DDGs inevitably become bulky and heavy implying high cost. Therefore, the economic incentive for a shift from geared systems to direct-drive systems seems insufficient [3].

In recent years, magnetically geared permanent magnet (MGPM) machines have received considerable attention [4]–[19]. MGPM machines incorporate a permanent magnet synchronous machine (PMSM) and a concentric-type magnetic gear (CMG) into one volume. Instead of physical teeth meshing as in mechanical gears, magnetic gears (MGs) transfer torque through the interaction of magnetic fields. Apart from their potential for high torque density, MGs further boast several important advantages resulting from their contact-less operation, namely (i) inherent overload protection, (ii) quiet operation, (iii) little maintenance, and (iv) high efficiency. It has been demonstrated that by integrating a PM machine with a CMG, a highly compact and torque dense machine can be realized [5]–[8], [10], [20]. For wind power applications, the drive-train configuration of an MGPM wind generator system is essentially the same as that of a DDG, as shown in Fig. 1.

This work was supported by ABB Corporate Research, Sweden.

The authors are with the Department of Electrical and Electronic Engineering, Stellenbosch University, Private Bag X1, Matieland 7602, South Africa (e-mails: 15894215@sun.ac.za; sgerber@sun.ac.za; rwang@sun.ac.za)

Manuscript received June xx, 2015; revised September xx, 2015.

Various topologies of MGPM machines such as axial flux [4], [17], inner-stator [9], [12], [16], outer-stator and wound modulator [14] have been proposed in literature. The outer-stator (OS) type MGPM machine was first described in [7], [8], which features a simpler mechanical structure than that of three air-gap MGPM machines [9], [12], [16]. A design strategy to ensure a well matched system between the CMG part and PM machine within an OS-MGPM machine was discussed in [15], which also investigated the influence of the design parameters on its torque capability. A simulation study on the transient behavior and steady-state performance of an OS-MGPM machine was reported in [13], which showed that the machine has a good power factor and low torque ripple. The design and analysis of an OS-MGPM machine specifically for naval applications was given in [11]. Although these studies covered important aspects on this type of MGPM machine, they mostly focused on theoretical analyses and simulations. The design procedure and optimization strategy of OS-MGPM machines has not been sufficiently treated in literature. There is also a lack of practical validation of this special machine to prove its potential benefits and identify its shortcomings for further improvement.

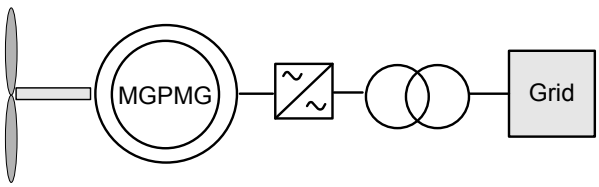

Fig. 1. Drive-train configuration of a MGPM wind turbine generator system.

In this paper, the fundamental operating theory of an OS-MGPM machine is briefly discussed. Then an efficient finite element method (FEM) based design optimization strategy is proposed and implemented in the design of such a machine. The design optimization focuses on maximizing torque per active mass within certain operational constraints. Based on the final design, a prototype is built and experimentally evaluated. The measured results are compared with those predicted by FEM, and relevant conclusions are drawn.

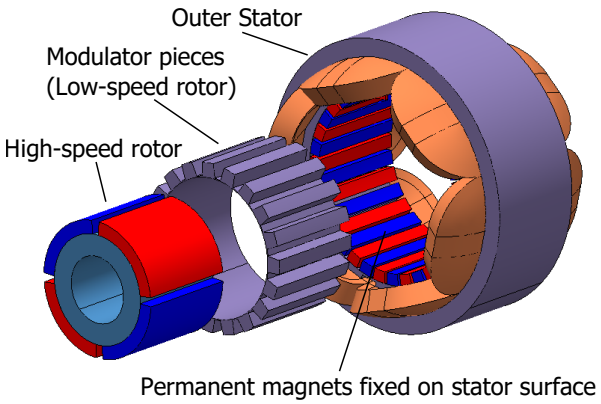

Fig. 2. The typical structure of an OS-MGPM machine.

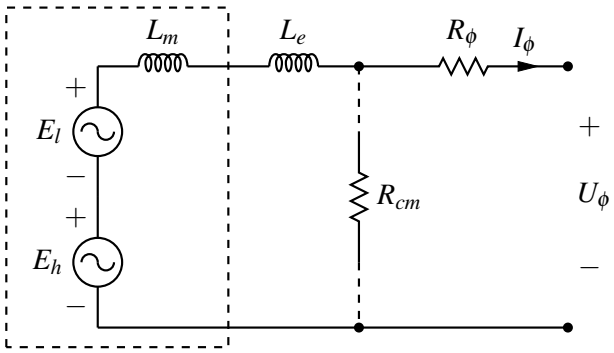

Fig. 3. Per-phase equivalent circuit of an OS-MGPM machine.

II. Outer-Stator MGPM Machine

The layout of an outer-stator MGPM machine is shown in Fig. 2. It comprises an inner high-speed (HS) PM rotor, a low-speed ferromagnetic rotor (flux modulator) and a tooth-wound outer-stator. Apart from carrying a balanced three-phase winding, the stator core also supports PMs on its bore surface. These PMs, together with the modulator and the high-speed rotor, form the CMG part of this machine. The stator and the high-speed rotor make up a synchronous PM machine. In this way, a CMG and a PM machine are magnetically and mechanically integrated into an MGPM machine. The high-speed rotor can be regarded as the coupling medium between the CMG and PM machine since it interacts with the magnetic field generated by the stator winding and the modulated field of the fixed PMs. As such, the machine contains two torque components during its operation:

- The *magnetic torque* that results from the magnetic gearing action of the HS rotor, flux modulator and PMs on the stator surface , just like in CMGs, and
- The *electromagnetic torque* which is developed, primarily, as a consequence of interaction between the HS rotor and the field generated by the stator windings as in PM synchronous machines.

A. Magnetic gearing principles

The *magnetic gearing principle* of CMGs relies on the use of ferromagnetic pole-pieces to modulate the magnetic fields generated by two sets of PMs. Each PM set produces a flux density distribution consisting of harmonic orders $p_{n,k}$ with angular speeds $\omega_{n,k}$ [21], [22]:

$$p_{n,k} = |np + kq_m| \tag{1}$$

$$\omega_{n,k} = \frac{np}{np + kq_m}\omega_h + \frac{kq_m}{np + kq_m}\omega_m \tag{2}$$

$$n = 1, 3, 5, ..., \qquad k = 0, \pm1, \pm2, \pm3, ..., \pm\infty$$

where p is number of pole-pairs of the PM rotor, ω_h and ω_m are the rotational speeds of the PM rotor and the modulator respectively, and q_m is number of modulator pole-pieces. The amplitude of the working harmonics are maximized when the number of pole-pairs on the inner and outer PM rotors, p_h and p_l, and q_m are related by [21]:

$$q_m = p_h + p_l \tag{3}$$

For an OS-MGPM machine such as shown in Fig. 2, the outer PM rotor is integrated with the stator and thus kept stationary. The gear ratio G_r between the inner PM rotor and the flux modulator is:

$$G_r = \frac{\omega_h}{\omega_m} = \frac{q_m}{p_h} = \frac{p_l}{p_h} + 1 \tag{4}$$

B. Equivalent circuit model

An MGPM machine is essentially a combination of a CMG and a PM machine. Its electrical equivalent circuit is largely the same as that of a PM synchronous machine with the exception that there is an additional magnetic excitation component from the gear side. Fig. 3 shows the per-phase equivalent circuit of an MGPM machine (for generating mode), in which E_h is the electromotive force (EMF) produced by the HS rotor PMs, E_l is the EMF due to the PMs on the stator surface and L_m, L_e and R_ϕ are the per-phase main inductance (including mutual inductance and all leakage inductance excluding end-winding inductance), end-winding inductance and resistance, respectively. The terminal voltage is U_ϕ and the phase current is I_ϕ. A shunt resistance R_{cm} can be included to account for core and magnet losses. Note that the set of PMs fixed on the stator surface has a different number of pole-pairs than the rotor and the stator winding. The flux responsible for the EMF induction is the result of the fundamental field harmonic from rotor PMs and the *modulated* harmonic from the fixed PMs, which has the same pole-pair number as the stator. The modulated harmonic from the fixed PMs usually has a much smaller amplitude than the fundamental from the rotor PMs and thus, the contribution to the EMF from the fixed PMs is small.

The performance calculation can be carried out by employing a field-circuit coupled approach described in [23]. As shown in Fig. 3, the part of the equivalent circuit marked by the dashed lines can be directly calculated using FEM whereas the remaining circuit parameters are computed analytically.

III. Design Optimization

A. Optimization strategy

The optimization of an MGPM machine can be regarded as a non-linear constrained problem that can be solved for various objectives. For wind generator applications, high torque capability and low weight are important design considerations. In this paper, the torque to active mass ratio of the machine is selected as the objective function, which is subjected to several design constraints. The optimization problem statement is formulated as:

$$\text{Maximize:} \quad F(\mathbf{X}) = \text{Torque } (T_m)/\text{active mass} \tag{5}$$

$$\text{Subject to:} \quad \gamma_i \geq 0.8 \tag{6}$$

$$t_{mh}/t_{ms} \leq 1.5 \tag{7}$$

$$J \leq 5\,\text{A/mm}^2 \tag{8}$$

where $\mathbf{X}$ represents the vector of design variables, consisting of the geometric variables illustrated in Fig. 4 and the current density. Constraint (6) states that the stator load factor [19] should be above 0.8. This factor is a measure of the relative torque capability of the stator and magnetic gear components of the machine. It is important to avoid an unbalanced design with either an oversized stator or an oversized MG. The constraint on the stator load factor ensures that PM machine and MG components of the MGPM machine are well matched. For an OS-MGPM machine, the stator load factor can be calculated as

$$\gamma_i = 1 + \frac{G_r T'_h}{T'_m} \tag{9}$$

with T'_h the torque on the HS rotor, and T'_m the stall torque on the modulator, both calculated with the machine operating at rated stator current and the gear's load angle [19] $\delta_g = 90°$. Note that the signs of T'_h and T'_m are opposite, and thus the second term in (9) is negative. Both T'_h and T'_m can be calculated from a single point finite element simulation, as described in [19]. The PMs on the stator surface are vulnerable to demagnetization due to the opposing magnetic fields from the inner rotor PMs and the currents in the stator coils. As a safety measure, the thickness ratio of the two PM sets is constrained in (7) to mitigate the potential demagnetization risk. In (8), the current density is limited to 5 A/mm^2 so that the MGPM machine can operate with natural air-cooling.

To reduce the prototype costs and facilitate the comparison with different types of MGPM machines, several design parameters of the machine shown in Table I are predefined for this study. The rated turbine speed was selected as 150 rpm, which is quite low for a small wind generator. However, our intended application is sub-25 kW small direct-drive wind power generators, which have a typical turbine speed around 150 rpm. The aim of this project is to develop a reduced scale prototype as a technology demonstrator.

B. Design environment

The flow diagram of a dedicated design optimization environment is demonstrated in Fig. 5, in which VisualDOC from VR&D Inc. is employed as the optimization toolbox that provides various optimization algorithms and couples with a

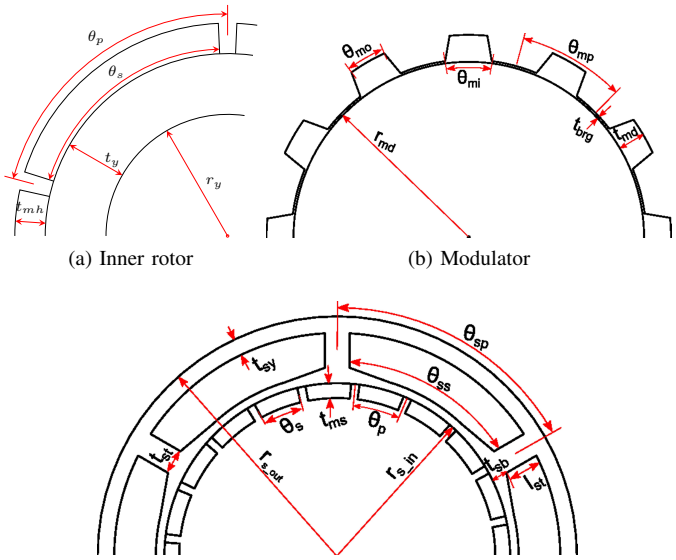

(a) Inner rotor (b) Modulator

(c) Stator and PMs on its surface

Fig. 4. Geometric variables input to FEM.

TABLE I
Fixed design parameters of the MGPM machine.

Outer diameter of the machine (mm)	140
Stack length of the machine (mm)	50
Air-gap length (mm)	0.7
Rated turbine speed (rpm)	150
Magnet remanence [T]	1.39
Magnet relative permeability	1.05
Lamination material	M470-50A

2D FE analysis program (SEMFEM) for single-point performance characterization. In this design, the modified method of feasible directions (MMFD) was applied to solve a predefined optimization problem. A 3D FE static solver is used in conjunction with a 2D FE transient solver to calibrate the performance of each optimum design by taking into account the 3D end-effects, PM and core losses.

C. Pole-slot selection

In the same manner as in conventional synchronous PM machines, the electromagnetic torque of an MGPM machine is developed as a result of interaction of mainly the high-speed rotor PMs' fundamental fields and stator windings. In addition, certain modulated harmonic fields originating from fixed PMs and having equivalent order to stator pole-pairs also contribute to this torque component. In a well balanced design, the electromagnetic torque can be amplified by a factor of G_r to the magnetic torque on the modulator, which significantly increases the machine's torque density. From a different perspective, G_r determines how much electromagnetic torque is required in order to harness a given input modulator torque. It can be seen from (4) that G_r is a function of p_h and p_l. Considering the winding factor and the dimensional constraints in Table I, the 4/6 and 6/9 appear to be two possible pole/slot combinations. Therefore, p_h can be either 2 or 3, while p_l remains to be determined.

To examine the relationship between the machine's torque capability and p_l, a design optimization study, which aims to

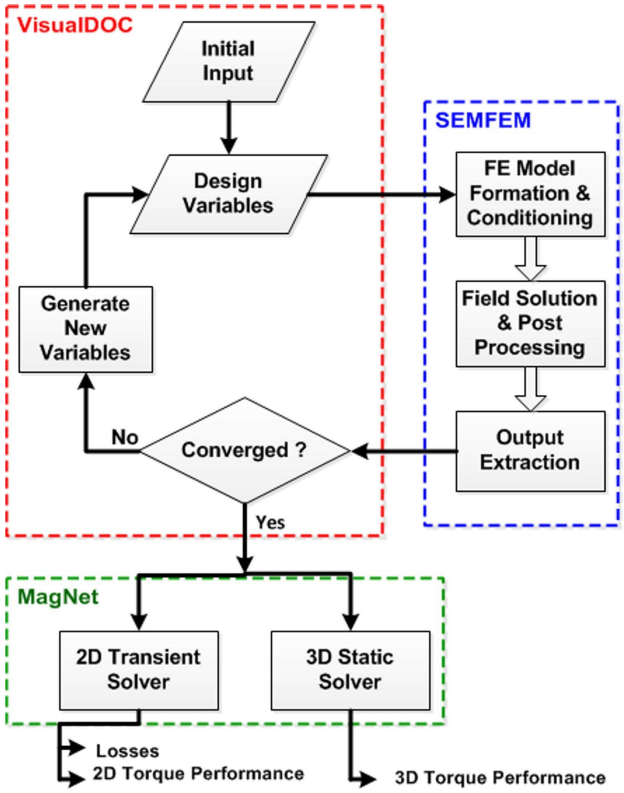

Fig. 5. Optimization flow diagram.

find the maximum torque value for a range of p_l numbers with p_h being 2 or 3, has been conducted. As shown in Fig. 6, a few interesting observations can be made: (i) the peak torque of the machine increases with p_l; (ii) for the same p_l number, the 4/6 combination invariably gives higher torque than that of 6/9 combination due to the reduced electromagnetic torque requirement resulting from higher G_r; (iii) the gradients of all the curves decline as p_l increases implying the existence of an optimum where further increase of p_l leads to insignificant gain in torque. This may be attributed to the severe leakage flux loss associated with the high number of PM poles. Based on the above, a final design with 4-pole ($p_h = 2$), 6-slot and $p_l = 19$ is considered the preferred option.

D. PM mass versus active mass

Since PM material makes a significant contribution to the total cost of an MGPM machine, the relationship between the PM mass and the total active mass is also investigated and given in Fig 7. Note that all the design points on the graph are individually optimized to satisfy the same output torque condition. It can be observed in Fig. 7 that (i) the total active mass of an MGPM machine can be brought down by using more PM material; (ii) a good trade off can be made between the two masses to realize a judicious design taking into account both cost and weight.

E. Final design

Table II summarizes the final values for the design variables defined in Fig. 4. Performance parameters and the active

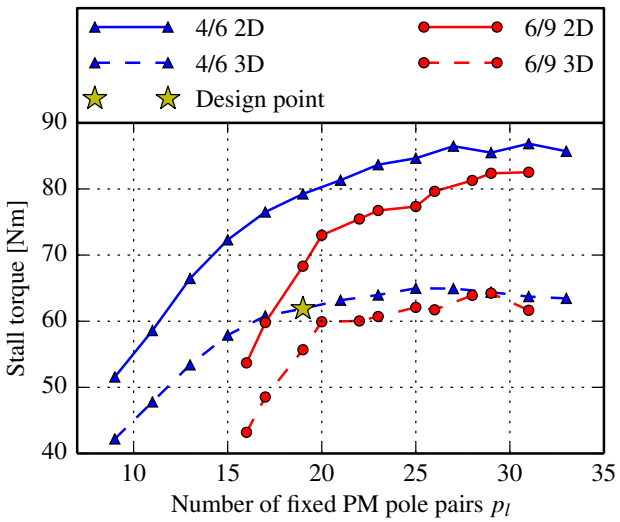

Fig. 6. Maximum torque as a function of stator magnet's pole number.

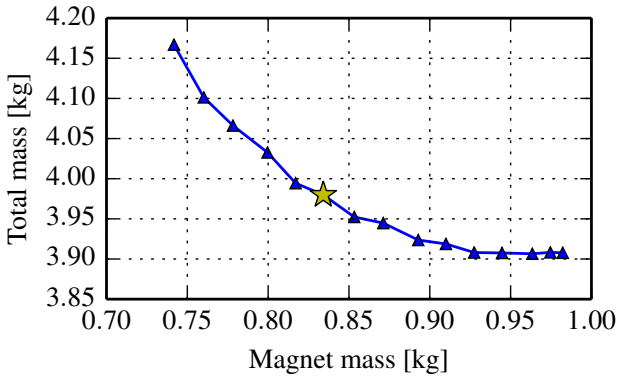

Fig. 7. Total active mass versus permanent magnet mass.

mass composition are given in Table III. The table highlights the difference between results obtained from 2D and 3D models. The large discrepancy of the 2D model is due to relatively long end-windings and severe end-effects associated with magnetic gears [10], [24], [25] and magnetically geared electrical machines [6], [26]. The 2D rated torque is related to the stall torque by the constraint on the stator load factor (6) while the rated current corresponds to a current density of 5 A/mm^2, satisfying (8). Due to the end-effects included in the 3D model, a higher stator load factor is realized in 3D results even with a slightly reduced current rating. The rated torque is chosen as 85% of the stall torque, allowing a margin to avoid slipping under normal operating conditions.

Since no special cogging torque minimization techniques were applied during the optimization, the cogging torque of the machine is relatively large.

The predicted machine efficiency based on 3D FEA is 90.8%, which is significantly lower than the 2D results where the losses in the end-windings are neglected. The computed loss components in the machine is given in Table IV. The stator makes a major percentage contribution to the losses due to the copper losses, whereas the frequency losses takes a small share because of relatively low operating frequency.

TABLE II
OPTIMIZED VARIABLES.

Parameter	Value	Units
Rotor magnet thickness (t_{mh})	6.50	mm
Fixed magnet thickness (t_{ms})	4.34	mm
Rotor magnet span to pole-pitch ratio (θ_s/θ_p)	0.92	–
Fixed magnet span to pole-pitch ratio (θ_s/θ_p)	0.84	–
Rotor yoke inner radius (r_y)	20.48	mm
Rotor yoke thickness (t_y)	11.71	mm
Modulator thickness (t_{md})	6.06	mm
Modulator bridge thickness (t_{brg})	0.5	mm
Inner modulator pole width ratio (θ_{mi}/θ_{mp})	0.50	–
Outer modulator pole width ratio (θ_{mo}/θ_{mp})	0.41	–
Stator tooth length (l_{st})	10.0	mm
Stator tooth thickness (t_{st})	7.27	mm
Stator tooth base thickness (t_{sb})	4.6	mm
Stator yoke thickness (t_{sy})	4.9	mm
Stator slot pole to pitch ratio (θ_{ss}/θ_{sp})	0.87	–
Stator slot fill factor (S_{ff})	0.55	–

TABLE III
KEY PARAMETERS AND PERFORMANCE OF THE MACHINE.

Descriptions	2D FEM*	3D FEM†	Units
Stall torque	76	61	Nm
Rated torque	62	52	Nm
Stator load factor γ_i	0.81	0.85	–
Stall torque density‡	99	79	kNm/m^3
Rated torque density‡	81	67	kNm/m^3
Stall torque per active mass	19.0	12.4	Nm/kg
Rated torque per active mass	15.5	10.6	Nm/kg
Cogging torque (peak-peak)	10.0	–	Nm
Torque ripple (peak-peak)	0.51	–	Nm
No-load phase voltage (rms)	139	133	V
Rated current (rms)	2.38	2.05	A
Rated speed (modulator)	150	150	rpm
Rated output power	917	744	W
Efficiency	94.2	90.8	%
Permanent magnet mass	0.834	0.834	kg
Copper mass	0.951	1.879	kg
Steel mass	2.209	2.209	kg
Total mass	3.994	4.922	kg

* Excl. end-winding.
† Incl. end-winding.
‡ Considering only active volume.

Based on the 2D FEA solution, the magnetic field and flux density distributions of the optimized machine under full-load conditions are shown in Fig. 8. The majority of the flux lines couple the stator, modulator and inner rotor across the two air-gaps, which is a beneficial and required circumstance for torque production and gearing purposes. However, there are a few other flux lines that form return paths between two adjacent PMs and/or the modulator, denoting the inter-pole leakage flux that negatively affects the machine's performance.

TABLE IV
LOSS COMPOSITION IN THE OS-MGPM MACHINE.

Component	Copper loss*	Hyst.-loss*	Eddy-loss*	Total*	%
Inner rotor	-	-	3.44	3.44	4.56
Modulator	-	1.76	0.50	2.26	3.0
Fixed PMs	-	-	3.11	3.11	4.13
Stator	59.2†	5.50	1.88	66.58	88.31
Total	59.2	7.26	8.93	75.39	-

* Loss reported in Watt.
† Incl. losses in the end-winding.

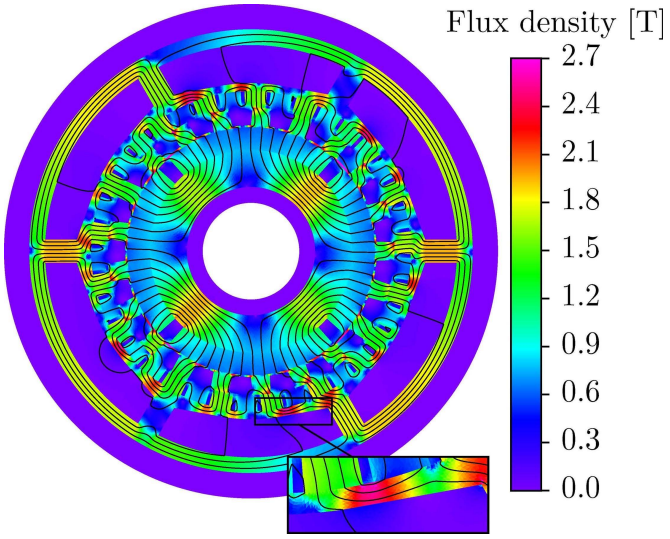

Fig. 8. Flux density and field lines under full load with rated stator current.

IV. MECHANICAL CONSTRUCTION

To facilitate the mounting of PMs on the inner surface of the stator, a closed-slot stator layout is chosen. Ideally, the teeth and the yoke of the stator are made separately (shown in Fig. 9a so that the preformed tooth coils can be inserted into the slots before fitting the teeth tightly inside the yoke. However, the assembly can also be challenging with a tight fit joint since both parts are made of steel laminations. It is thus decided to adopt a totally closed slot stator shown in Fig. 9b for the prototype machine. As shown in Fig. 8, the bridges of the closed slot are magnetically saturated. Owing to the difficult winding process, a poor stator slot fill factor of 0.36 was realized, which increases the copper losses in the stator winding. The flux modulating ring was also made out of non-oriented Silicon-steel laminations in order to minimize the frequency dependent iron losses in this component. Besides requirements to limit losses, the modulator is susceptible to strong magnetic forces resulting from both sets of PMs. Thus certain strategies had to be implemented to preserve its mechanical integrity even during over-loaded conditions. Firstly, the fully assembled modulator is supported from both sides with hubs to keep it concentric and perfectly aligned with the inner rotor despite continuously varying forces. The thin bridges connecting the modulator pole-pieces actually serves two major purposes, that is, they filter out some of the undesired flux harmonics, thereby reducing torque ripples and losses [10], [25], [27], while also holding the pole-pieces together at an equal angular distance from each other. In order to keep the stack of laminations intact, they are compressed by two end hubs and stainless steel rods running in their slots. Since stainless steel is electrically conductive, one supporting hub was made from a hard plastic material to avoid turning the modulator into a squirrel cage rotor. To further strengthen the modulator, an epoxy resin was filled in the remaining air-spaces between the laminations and the rods. Figure 10a shows the model of the modulator with all supporting pieces in place and the actual manufactured component in Fig. 10b.

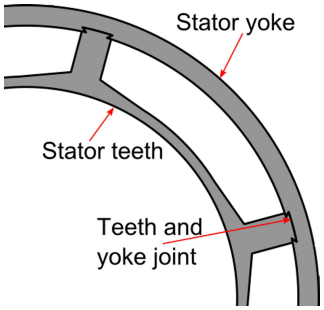

(a)

(b)

Fig. 9. Stator design options. (a) Two-part stator. (b) Closed slot stator.

As depicted, the aluminum hub, laminations and rods are all united into one component by the epoxy resin. Figure 11a shows the longitudinal section of the complete machine which illustrates the mechanical arrangement of components, and the Fig. 11b shows the assembled prototype. A temperature sensor is embedded in the region between the coils and part of the stator holding the PMs to monitor their temperatures during operation.

V. Experimental Evaluation

The performance of the outer-stator MGPM prototype was evaluated experimentally in order to validate the simulated results. The test setup is shown in Fig. 12. The prototype is driven at a required speed by the servo motor while a torque sensor measures the input speed, torque and power. The prototype's load consists of a three-phase star-connected resistor bank connected through an auto-transformer.

A. No-load voltage

The open-circuit characteristics of the machine are experimentally determined by operating it as a generator under a no-load condition. The three-phase no-load output voltage measurements obtained at a speed of 150 rpm is shown in Fig. 13, along with simulated waveforms. It can be seen that the waveform is non-sinusoidal due to the large fifth harmonic produced by the prototype's winding configuration. The amplitude of the experimental voltage waveform is lower (by about 7%) than that of the FE simulated one. Apart from the discrepancies in induced voltage magnitudes, the measured and simulated waveforms closely resemble each other.

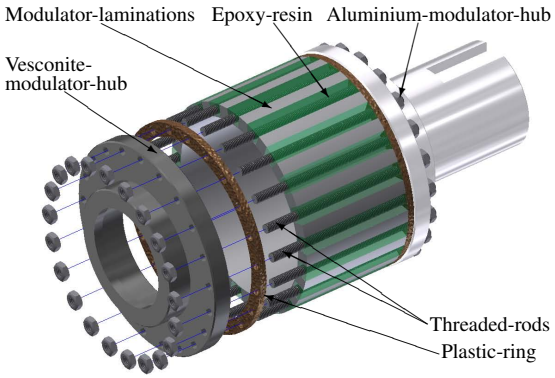

(a)

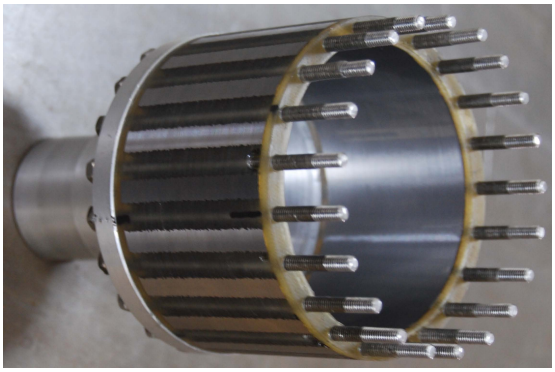

(b)

Fig. 10. Modulator design. (a) Modulator structure and support components. (b) Manufactured component.

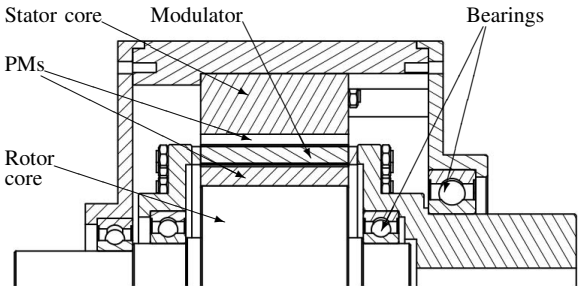

(a)

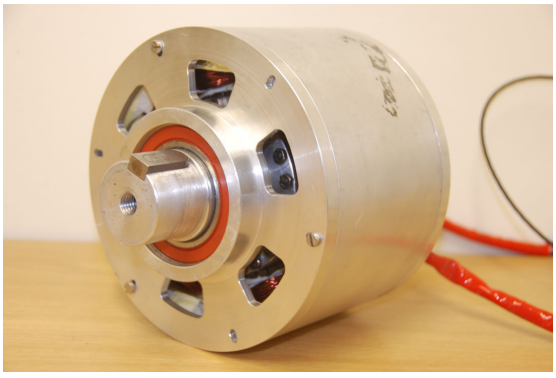

(b)

Fig. 11. The prototype MGPM machine. (a) Mechanical layout (Longitudinal section). (b) Assembled prototype.

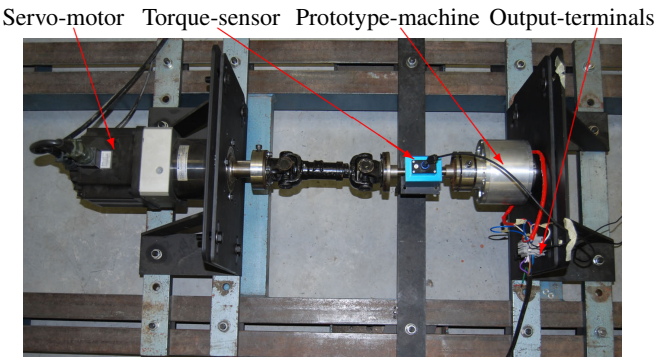

Fig. 12. Test bench setup used to evaluate the prototype.

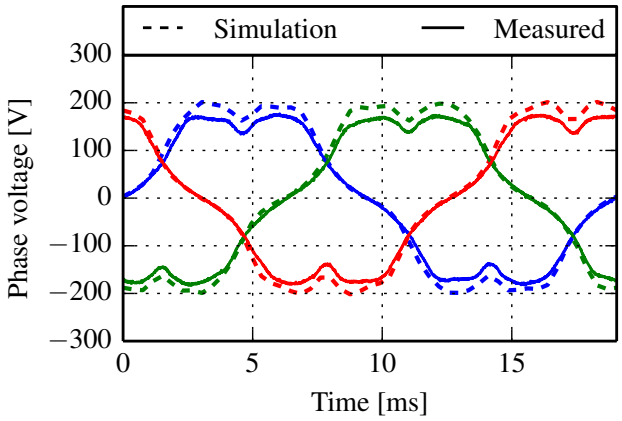

Fig. 13. Open circuit voltage waveforms at 150 rpm.

The no-load back-EMF measurements were also carried out at various speeds. Figure 14 shows a graph of the magnitude of the experimental and simulated back-EMFs as a function of speed. The 2D-FEM simulated results are slightly higher than the measured values.

B. No-load losses

The machine's no-load power loss was also investigated at different rotational speeds and higher than expected losses were measured. The no-load power loss consists of core loss in the laminated components, eddy-current loss in solid

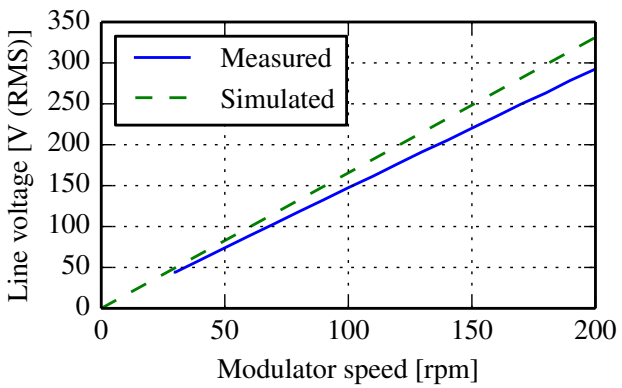

Fig. 14. Line rms voltage as function of speed.

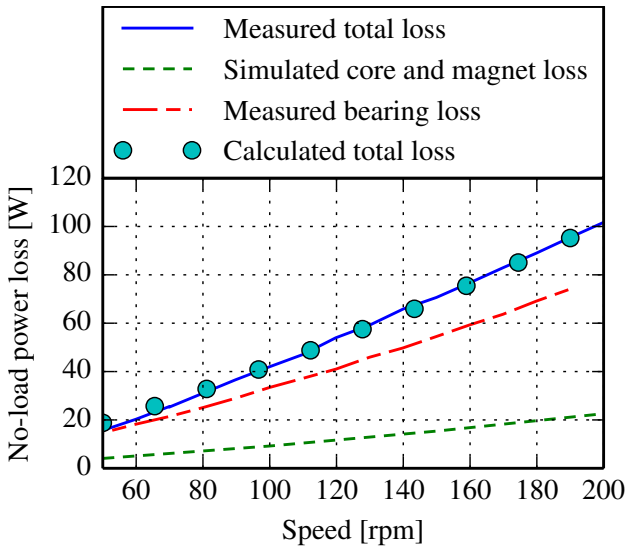

Fig. 15. Breakdown of the no-load loss components at different speeds.

components and windage and bearing loss. After observing rather large changes in the no-load losses when loosening some nuts that place a preload on the bearings, the bearing loss was investigated further. The machine was disassembled and the bearings were tested individually. A test model excluding the electrical or electromagnetic active parts of the machine was constructed and the bearings tested at different speeds up to the machine's rated speed. A breakdown of the no-load losses at different speeds are given in Fig. 15, which shows that the bearings largely contributed to the no-load losses. The reason for the high bearing loss could be poor quality bearings and the fact that the bearings seem to be over-sized relative to the machine size. This means the mechanical structure (which was not the focus of this machine optimization) needs to be improved in the future.

C. Stall torque

The maximum static torque or stall torque of the magnetic gear part of the machine was measured by locking the inner PM rotor while the modulator was rotated step-wise. The obtained experimental results are presented in Fig. 16, along with the 3D FEM simulated torque vs load angle curve. The two curves compare favorably with the maximum simulated and experimental torques equal to 61 Nm and 59 Nm respectively, a difference less than 4%.

D. Cogging torque

One disadvantage of the MGPM machine is that the effective cogging torque on the modulator is usually dominated by an amplified version of the cogging torque on the high-speed rotor due to its interaction with the stator slots when the machine is at standstill or running at very low speeds. At higher speeds, however, this amplification is reduced because the high-speed rotor inertia prevents large oscillations in its position. The measured cogging torque at standstill is given in Fig. 17, along with a calculated waveform. The peak-to-peak amplitude of 10 Nm is roughly 16% of the machine's

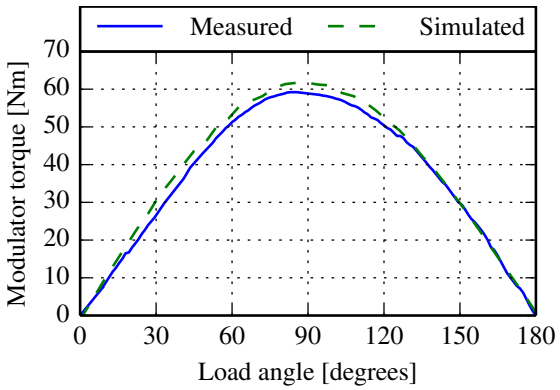

Fig. 16. Stall torque vs. load angle curves.

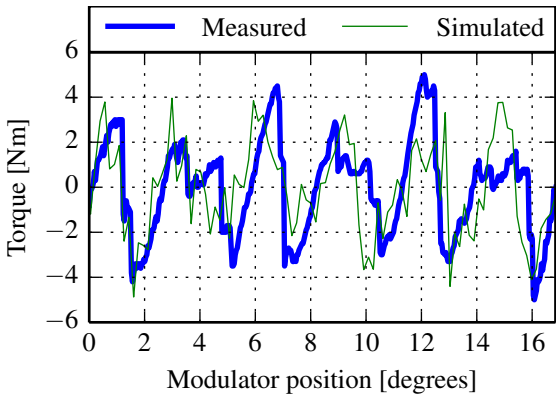

Fig. 17. Cogging torque characteristics of outer stator MGPM machine.

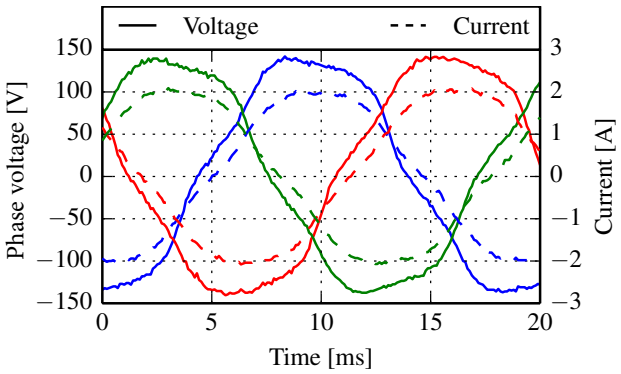

Fig. 18. Output voltage and current at 150 rpm and 75% of rated load.

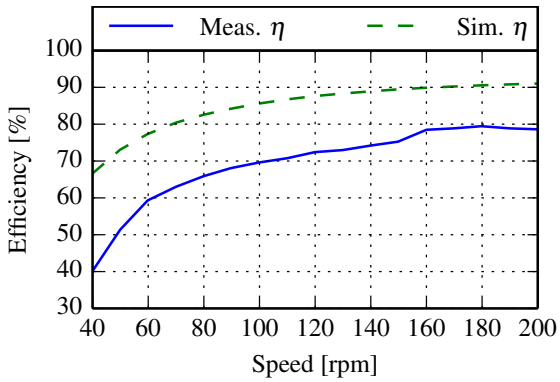

Fig. 19. Predicted and measured efficiency as function of speed.

stall torque. In contrast, the peak-to-peak no-load torque ripple due to cogging effects is expected to be a mere 0.51 Nm when there are no oscillations in the magnetic gear's load angle (high-speed operation). This is due to the fact that the lowest common multiple (LCM) between the number of modulator segments and the number of high-speed rotor poles, fixed PMs and stator teeth are all quite high.

E. Load tests

The machine's output voltage and current waveforms at 150 rpm and roughly 75% of rated load are presented in Fig. 18. The measured power factor is about 0.95. To determine the efficiency of the machine, the mechanical input and electrical output powers are measured at various operating speeds and loads. All tests were conducted at a power factor above 0.92, demonstrating that the machine can operate at a high power factor over its operational range. A comparison between the measured and predicted efficiency at rated current is made in Fig. 19. The measured efficiency is significantly lower than the predicted one due to the high no-load losses and the poor fill factor that was realized. Since the machine's operating efficiency varies with both the operating speed and load, it is useful to show the efficiency under various operating conditions. Therefore, further measurements were carried out to construct an efficiency map for a better evaluation of the machine's performance. Fig. 20 is the measured efficiency map of the prototype machine. It can be observed that the efficiency increases at higher speeds. Looking from perspective of the load at fixed speed, the efficiency increases with load reaching a peak point after which further increase leads to a drop in efficiency. At high loads, the copper loss increases more rapidly than the torque.

F. Thermal and demagnetization analysis

The thermal performance of the machine was evaluated by injecting the rated current in DC, corresponding to copper losses of 60 W, and recording the readings from temperature sensors embedded in the winding and on the outer surface of the machine's casing. To eliminate the influence of excessive

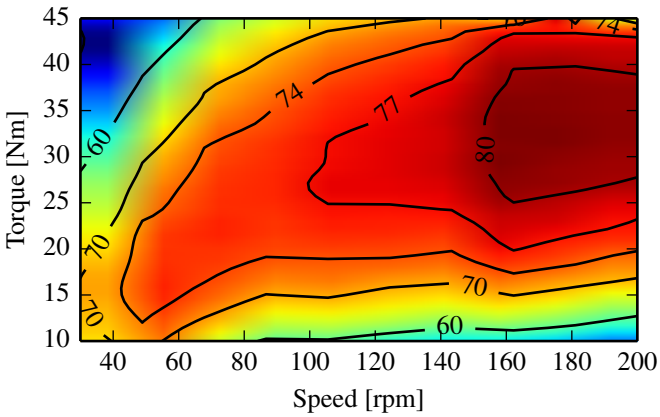

Fig. 20. Efficiency map of input speed and torque.

bearing losses, the machine was at standstill during the test, which explains the longer thermal time constant of such a small machine. Fig. 21 shows how the temperatures rise over time until the steady-state values are reached. From this test, it can be clearly seen that the temperature rise in the winding is approximately 60°C at rated operating conditions. Fig. 22 shows a thermal image of the inside of the machine taken through a "window" in the casing at the end of the test period. It shows that the temperature of the magnets on the stator surface is approximately 70°C. This is important information for demagnetization analyses. Similar to conventional PM wind generators, the consequences of an MGPM generator under different operating conditions along with demagnetizing effects on PMs are important design aspects. Three scenarios were investigated in order to assess the demagnetization risks in the machine. In Fig. 23, the demagnetization proximity of the magnets, according to 2D FEA, is shown for the three cases. These simulations were conducted assuming that the magnets' temperature was 80°C and that demagnetization occurs if the flux density drops below 0.3 T in the direction of magnetization, which corresponds to the knee point of the demagnetization curve. In these figures, red (light color if in grayscale) indicates areas where the flux density has dropped more than 0.1 T below the demagnetization point whereas blue (dark color if in grayscale) represents areas where the flux density is more than 0.1 T above the demagnetization point. Fig. 23a shows that under short-circuit conditions, the risk of demagnetization is actually low, despite a short-circuit current of 2.3 per unit, contrary to what occurs in conventional PM machines. In this magnetically geared machine, the primary risk of demagnetization is due to the strong field from the high-speed rotor demagnetizing the stator magnets. Under short-circuit conditions, the field from the high-speed rotor magnets is actually weakened, reducing the demagnetization risk. Fig. 23b illustrates the situation under full-load operating conditions. The analysis shows that the inner corners of the magnets may be susceptible to demagnetization under these conditions. However, the worst case among the three scenarios considered is the third. In this case, the machine's gear load angle $\delta_g = 180°$, which means that fields from the high-speed rotor and the stator PMs oppose each other, and rated positive d-axis current is injected. This scenario may occur if the machine is overloaded, the magnetic gear slips and an incorrect current angle is applied. Fig. 23c shows that these conditions result in the highest demagnetization risk and should be considered in the design of such machines.

VI. Conclusion

This paper has presented the design optimization of an outer stator MGPM machine with the objective of maximizing the torque per active mass. It has been shown that careful selection of suitable pole-pair combinations for both the stator and MG are important as it directly affects the machine's gear ratio, torque capacity and quality. Furthermore, a trade-off has to be made between PM mass and total mass of the machine as they are inversely proportional to each other.

A prototype machine was constructed from the optimized parameters and tested. The measured torque performance

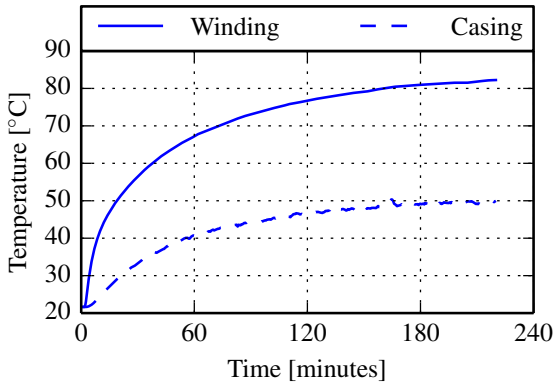

Fig. 21. Temperature of the winding and the outer surface of the casing (Ambient temperature: 22°C).

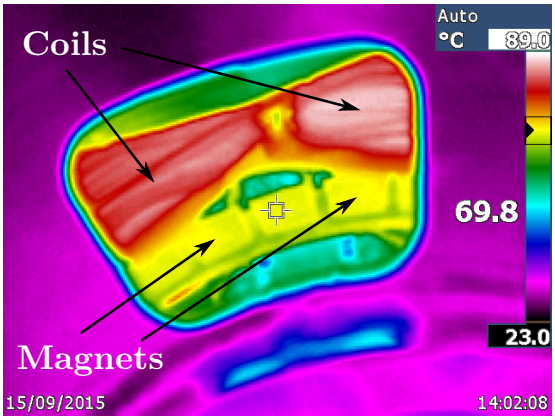

Fig. 22. Thermal image of the inside of the prototype at thermal equilibrium.

compares favorably with the predicted ones, which shows that the design approach is accurate. However, the measured efficiency differs from the calculated results by a significant margin. This difference is attributed to higher than expected no-load loss and the poor fill factor that was realized. It was found that bearing loss was largely responsible for the high no-load loss. The mechanical design should be revisited to reduce these unwanted losses.

In addition, the thermal performance of the machine has also been evaluated. It shows that the MGPM machine prototype can safely operate under rated condition with natural cooling. Detailed demagnetization analyses were also performed for different operating conditions.

The machine is most prone to demagnetization when the magnetic gear slips. This overload protection mechanism is often held as an advantage of MGPM machines, but the analysis shows that it is important to consider this condition in the design to avoid demagnetization.

References

[1] H. Polinder, F. van der Pijl, G.-J. de Vilder, and P. Tavner, "Comparison of direct-drive and geared generator concepts for wind turbines," *IEEE Trans. Energy Conversion*, vol. 21, no. 3, pp. 725–733, Sept 2006.

[2] R.-J. Wang and S. Gerber, "Magnetically geared wind generator technologies: Opportunities and challenges," *Applied Energy*, vol. 136, pp. 817–826, Dec 2014.

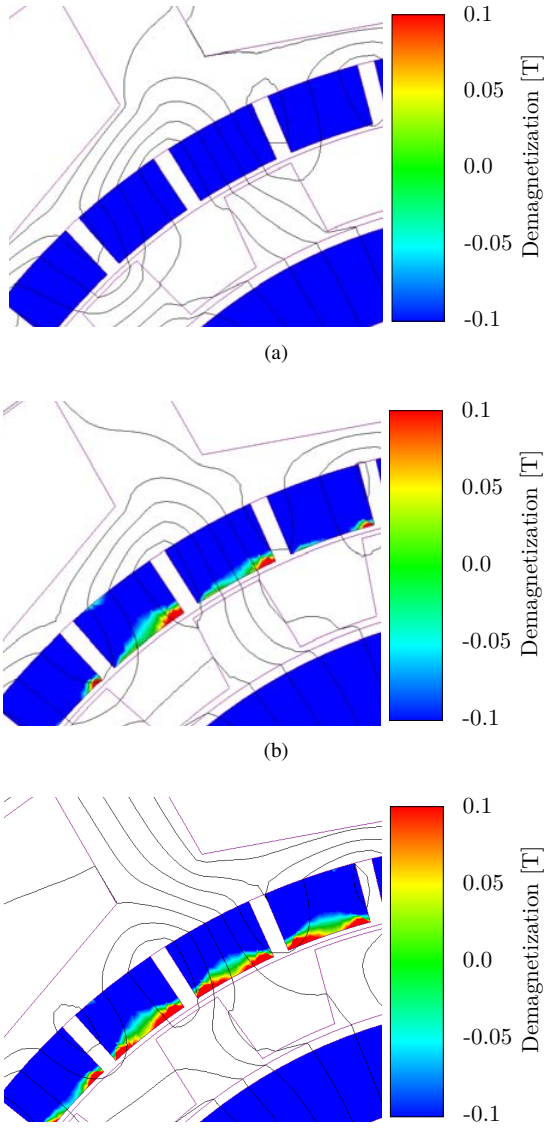

Fig. 23. Demagnetization analyses of the machine under various conditions: (a) Short-circuit. (b) Full-load operation. (c) Slipping with $\delta_g = 180°$ and rated positive d-axis current.

[3] D. McMillan and G.W. Ault, "Techno-economic comparison of operational aspects for direct drive and gearbox-driven wind turbines," *IEEE Trans. Energy Conversion*, vol. 25, no. 1, pp. 191–198, Mar 2010.

[4] M. Venturini and F. Leonardi, "High torque, low speed joint actuator based on PM brushless motor and magnetic gearing," in *Proc. of IEEE Industry Applications Society Annual Meeting*, Toronto, Canada, 2-8 Oct 1993, vol. 1, pp. 37–42.

[5] A. Razzell and J. Cullen, "Compact electrical machine," US Pat. 6 794 781B2, 2004.

[6] K. Chau, D. Zhang, J. Jiang, C. Liu, and Y. Zhang, "Design of a magnetic-geared outer-rotor permanent-magnet brushless motor for electric vehicles," *IEEE Trans. Magn.*, vol. 43, no. 6, pp. 2504–2506, June 2007.

[7] K. Atallah, S. Calverley, R. Clark, J. Rens, and D. Howe, "A new PM machine topology for low-speed, high-torque drives," in *Proc. of 18th International Conference on Electrical Machines (ICEM 2008)*, Vilamoura, Portugal, 6-9 Sept 2008, pp. 1–4.

[8] K. Atallah, J. Rens, S. Mezani, and D. Howe, "A novel "pseudo" direct-drive brushless permanent magnet machine," *IEEE Trans. Magn.*, vol. 44, no. 11, pp. 4349–4352, Nov 2008.

[9] S. Du, Y. Zhang, and J. Jiang, "Research on a novel combined permanent magnet electrical machine," in *Proc. of International Conference on Electrical Machines and Systems (ICEMS 2008)*, Wuhan, China, 17-20 Oct 2008, pp. 3564–3567.

[10] P. Rasmussen, H.H. Mortensen, T. Matzen, T. Jahns, and H. Toliyat, "Motor integrated permanent magnet gear with a wide torque-speed range," in *Proc. of IEEE Energy Conversion Congress and Exposition (ECCE 2009)*, San Jose, CA, 20-24 Sept 2009, pp. 1510–1518.

[11] D. Powell, S. Calverley, F. de Wildt, and K. Daffey, "Design and analysis of a pseudo direct-drive propulsion motor," in *5th IET International Conference on Power Electronics, Machines and Drives (PEMD 2010)*, Brighton, UK, 19-21 Apr 2010, pp. 1–2.

[12] L. Jian, K. Chau, and J. Jiang, "An integrated magnetic-geared permanent-magnet in-wheel motor drive for electric vehicles," in *IEEE Vehicle Power and Propulsion Conference (VPPC 2008)*, Harbin, China, 3-5 Sept 2008, pp. 1–6.

[13] S. Ho, S. Niu, and W. Fu, "Transient analysis of a magnetic gear integrated brushless permanent magnet machine using circuit-field-motion coupled time-stepping finite element method," *IEEE Trans. Magn.*, vol. 46, no. 6, pp. 2074–2077, June 2010.

[14] L. Jian, G. Xu, Y. Gong, J. Song, J. Liang, and M. Chang, "Electromagnetic design and analysis of a novel magnetic gear integrated wind power generator using time-stepping finite element method," *Progress In Electromagnetics Research*, vol. 113, pp. 351–367, 2011.

[15] D.J. Evans and Z. Zhu, "Optimal torque matching of a magnetic gear within a permanent magnet machine," in *Proc. of IEEE International Electric Machines Drives Conference (IEMDC 2011)*, Niagara Falls, Canada, 15-18 May 2011, pp. 995–1000.

[16] P. Rasmussen, T. Frandsen, K. Jensen, and K. Jessen, "Experimental evaluation of a motor-integrated permanent-magnet gear," *IEEE Trans. Ind. Appl.*, vol. 49, no. 2, pp. 850–859, March 2013.

[17] R.-J. Wang, L. Brönn, S. Gerber, and P. Tlali, "Design and evaluation of a disc-type magnetically geared PM wind generator," in *Proc. of 4th International Conference on Power Engineering, Energy and Electrical Drives (POWERENG 2013)*, Istanbul, Turkey, 13-17 May 2013, pp. 1259–1264.

[18] P. Tlali, R.-J. Wang, and S. Gerber, "Magnetic gear technologies: A review," in *Proc. of International Conference on Electrical Machines (ICEM 2014)*, Berlin, Germany, 2-5 Sept 2014, pp. 544–550.

[19] S. Gerber and R.-J. Wang, "Design and evaluation of a magnetically geared PM machine," *IEEE Trans. Magn.*, vol. 51, no. 8, 10p, 2015.

[20] L. Jian, K. Chau, and J. Jiang, "A magnetic-geared outer-rotor permanent-magnet brushless machine for wind power generation," *IEEE Trans. Ind. Appl.*, vol. 45, no. 3, pp. 954–962, May 2009.

[21] K. Atallah and D. Howe, "A novel high-performance magnetic gear," *IEEE Trans. Magn.*, vol. 37, no. 4, pp. 2844–2846, Jul 2001.

[22] K. Atallah, J. Wang, and D. Howe, "A high-performance linear magnetic gear," *Journal of Applied Physics*, vol. 97, no. 10, pp. 10N516–10N516–3, May 2005.

[23] R.-J. Wang, M. Kamper, K. Van der Westhuizen, and J. Gieras, "Optimal design of a coreless stator axial flux permanent magnet generator," *IEEE Trans. Magn.*, vol. 41, no. 1, pp. 55–64, Jan. 2005.

[24] P. Rasmussen, T. Andersen, F. Jorgensen, and O. Nielsen, "Development of a high-performance magnetic gear," *IEEE Trans. Ind. Appl.*, vol. 41, no. 3, pp. 764–770, May 2005.

[25] S. Gerber and R.-J. Wang, "Evaluation of a prototype magnetic gear," in *Proc. of IEEE International Conference on Industrial Technology (ICIT 2013)*, Cape Town, South Africa, 25-28 Feb 2013, pp. 319–324.

[26] S. Gerber and R.-J. Wang, "Analysis of the end-effects in magnetic gears and magnetically geared machines." *Proc. of Internationl Conference on Electrical Machines (ICEM 2014)*, Berlin, Germany, 2-5 Sept 2014, pp. 396–402.

[27] N. Frank and H. Toliyat, "Analysis of the concentric planetary magnetic gear with strengthened stator and interior permanent magnet (IPM) inner rotor," in *Proc. of IEEE Energy Conversion Congress and Exposition (ECCE 2010)*, Atlanta, GA, 12-16 Sept 2010, pp. 2977–2984.